Direct visualization of distorted twin boundaries in Ce-doped

GdFeO₃

Ke Ran, a,b* Juri Barthel, b Lei Jin, b Daesung Park, Annika Buchheit, Kerstin Neuhaus, d Stefan

Baumann, e Wilhelm A. Meulenberg, e,f Joachim Mayer a,b

^a Central Facility for Electron Microscopy GFE, RWTH Aachen University, 52074 Aachen, Germany.

^b Ernst Ruska-Centre for Microscopy and Spectroscopy with Electrons ER-C, Forschungszentrum Jülich GmbH,

52425 Jülich, Germany.

^c Physikalisch-Technische Bundesanstalt PTB, 38116 Braunschweig, Germany

^d Institute of Energy and Climate Research IEK-12, Forschungszentrum Jülich GmbH, 48149 Münster, Germany

e Institute of Energy and Climate Research IEK-1, Forschungszentrum Jülich GmbH, 52425 Jülich, Germany

^f Faculty of Science and Technology, Inorganic Membranes, University of Twente, 7500 AE Enschede, The

Netherlands

* Correspondence: ran@gfe.rwth-aachen.de

Abstract

Utilizing advanced transmission electron microscopy (TEM), the structure at the (110) type twin

boundary (TB) of Ce-doped GdFeO₃ (C-GFO) has been investigated with picometer precision.

Such a TB is promising to generate local ferroelectricity within a paraelectric system, while

precise knowledge about its structure is still largely missing. In this work, a direct measurement

of the cation off-centering with respect to the neighboring oxygen is enabled by integrated

differential phase contrast (iDPC) imaging, and up to 30 pm Gd off-centering is highly localized

at the TB. Further electron energy loss spectroscopy (EELS) analysis demonstrates a slight

accumulation of oxygen vacancies at the TB, a self-balanced behavior of Ce at the Gd sites,

and a mixed occupation of Fe²⁺ and Fe³⁺ at the Fe sites. Our results provide an informative

picture with atomic details at the TB of C-GFO, which is indispensable to further push the

potential of grain boundary engineering.

Keywords

Ferroelastic twin boundary, GdFeO₃, STEM-HAADF, iDPC, EDX, EELS

Domain boundaries can be functional elements of a material while the same functionality does not exist in the bulk.¹ It was the discovery of superconducting twin boundaries (TB) in WO₃,² that opened a wide field of application "domain boundary engineering". Thereafter, continuous research efforts have been motivated, to tailor the boundaries with desired properties and reproducing them in an engineering fashion. Successful examples include BiFeO₃,³ where the formation of a dopant-controlled polar pattern was able to cause periodic giant polarization gradients. Moreover, the ferroelectricity in various heterostructures, such as CaTiO₃/BaTiO₃ and PbZr_{0.2}Ti_{0.8}O₃/SrRuO₃,⁴⁻⁷ can be effectively tuned by surface and interface strains as well.

The observation of TB related polarity⁸⁻¹² leads to new directions to produce complex patterns in the bulk for ferroic devices. Within a paraelectric CaTiO₃ matrix, ferrielectricity was predicted at the (110) type TB, resulting from distorted TiO₆ octahedra with the Ti slightly off the geometrical midpoint. 10, 12 Such TBs are then considered as promising elements for ferroelectric devices, given that their density and therefore the device performance can be pushed via boundary engineering. Besides, it is also expected, that oxygen vacancies are rather uniformly distributed within the TB but depleted in the bulk. 13 However, neither the Ti off-centering nor the oxygen vacancies have been directly observed by experiment. Yet, this is indispensable information for a precise understanding of the TB-related properties, and a critical premise for a successful TB engineering. Therefore, the present study focuses on a (110) type TB formed in the Ce-doped GdFeO₃ (C-GFO). The C-GFO in our case is identified as a secondary phase within the Gd- and Fe-doped ceria, 14 and Ce is partially occupying Gd sites. Among the various applications of C-GFO, an important one is boosting the overall performance of dual phase oxygen membranes, by tuning the electronic characteristics of C-GFO through Ce substitution of Gd. 15 Both GFO and CaTiO₃ belong to the space group Pbnm, and the same (110) type TB enables a direct comparison between the two cases and sound references for similar systems.

Transmission electron microscopy (TEM) with sub-Ångström resolution provides unique advantages in studying the local atomic structure and chemical composition. The C-GFO in

our study is imaged along the [001] direction in order to maximize the visibility of any structural distortion related to the TB, except along the viewing direction. In addition to high-angle annular dark-field (HAADF) imaging, we also apply the integrated differential phase contrast (iDPC) technique¹⁷, which allows us to analyze both light and heavy elements from the same data. Relative shifts of both cations, namely Gd and Fe, are observed from the center of symmetry. This polar feature is mainly found for Gd with up to 30 pm Gd off-centering exclusively at the TB. In addition, the TB shifts at the nanometer scale whereas no significant inclination is observed on a macroscopic level. Moreover, chemical variation in the vicinity of the TB is probed by both energy dispersive X-ray (EDX) and electron energy loss spectroscopy (EELS). With this comprehensive characterization down to pm scale enabled by advanced TEM techniques, indispensable insights into the emerging polarity at the TB of the paraelectric C-GFO are obtained for the first time.

The C-GFO grain studied in this work is shown in Fig. 1a. It is ~1 µm in size and surrounded by the ceria host phase. As denoted by the pair of arrows in cyan, the TB is almost straight, going through the grain, and dividing the grain into a smaller upper (U) and a larger lower (L) part. Additional stacking faults are also noticed in the U part, and marked by the two arrows in pink, which will be discussed in a separate study. By selecting the region defined by the dotted circle in Fig. 1a, the diffraction pattern in Fig. 1b was acquired. As outlined by the red and blue rectangles in Fig. 1b, two identical patterns with a relative rotation of ~87° can be recognized. Both patterns are further indexed as along [001] direction of the GFO structure, as shown in Fig. 1c, and corresponding to the U and L part, respectively (Supporting Information, Fig. S1).

The averaged HAADF image in Fig. 1c resolves the cation sub-lattice at the TB in projection along [001]. The peaks of higher intensity correspond to Gd/Ce atomic columns while the lower intensity peaks occur at the positions of Fe-O columns, as the heavier Gd/Ce columns appear brighter than the lighter Fe-O columns in the Z-contrast image. On the right side of Fig. 1d is the laterally averaged intensity from the HAADF image. Clearly, a single Gd {110} plane in the middle (the TB plane as marked by the arrow), is showing a higher intensity and separates the

U and L parts. As shown in Fig. 1c, the two neighboring Gd atomic columns at each Gd positions are separated by ~68 pm. Thus, in the bulk region, elliptical peak shapes are found consistently at the Gd/Ce positions, and a mean ellipticity of ~1.4 can be determined. 18 Meanwhile, at the TB, the ellipticity of Gd/Ce peaks alternates between approximately 1.1 and 1.4 (Supporting Information, Fig. S2). Mimicking all the experimental observations and ignoring the Ce substitution of Gd, a structural model of the TB is proposed, and overlaid on the HAADF image in Fig. 1d. To build the model, a relative rotation of ~87° and a translation of ½[11-1] between the U and L part are introduced. Moreover, atomic reconstruction along the TB is considered, in order to account for the varying shapes and lattice constants detected at the TB as discussed below and in Supporting Information, Fig. S3. The right inset in Fig. 1d is the simulated HAADF image based on the proposed model. 19 Qualitatively, a good agreement between the experiment and simulation is reached, where a stronger channeling effect at the reconstructed TB is likely to cause the brighter TB in HAADF imaging (Supporting Information, Fig. S3).

Fig. 1e shows the EDX chemical mapping results around the TB, including the simultaneously acquired HAADF image, extracted elemental maps using Gd $L\alpha$, Fe $K\alpha$, Ce $L\alpha$ and O K line, together with a composite map of Gd and Fe. The Gd and Fe map fit nicely with the model overlaid on the HAADF image. Several local maxima are recognizable in the Ce map, and coincide with some of the Gd sites, as suggested by the two sets of dotted squares which are placed at the same positions in the Gd and Ce map, respectively. Consistent with the EELS spectrum imaging (EELS SI) results (discussed below), an effective Ce substitution of Gd can be identified. Moreover, across the TB, no significant intensity variation can be noticed in either the Gd, Fe or the Ce maps. The composite map of Gd and Fe in Fig. 1e also verifies a uniform intensity distribution in the vicinity of the TB.

Furthermore, although a macroscopic straight behavior of the TB is revealed in Fig. 1a, the TB in our study also shifts, i.e. plane by plane between the U and L part, similar as those observed in the Pb(Zr,Ti)O₃ and LiNbO₃ thin films.^{20,21} Shifts of TB between neighboring Gd {110} planes

results in kinks (Supporting Information, Fig. S4), which are observed with varying densities, but behave stable under our experimental condition (Supporting Information, Fig. S5-6).

For further structural analysis, the averaged HAADF image in Fig. 2a with a larger field of view is selected. As shown in Fig. 2a, the pseudo lattice constant ap and bp are defined and determined for the Gd and Fe sub-lattice, respectively. Using two-dimensional Gaussian fitting, 18 the Gd and Fe positions are first determined (measurement precision ~5 pm). Taking the two outlined regions in Fig. 2a as a reference, Fig. 2b-c and 2d-e map deviations Δa_p and Δb_p from the bulk for each sub-lattice. Significant deviations $\Delta a_{p,Gd}$ of the Gd sub-lattice are detected along row #12 (the TB) and plotted in Fig. 2b. On the right side of Fig. 2b we plot the averaged Δa_{p,Gd} from each Gd row, where the value at row #12 is slightly above zero and with a larger standard deviation. Fig. 2f further plots the individual $\Delta a_{p,Gd}$ from row #12 ($\Delta a_{p,Gd,12}$), which is oscillating around zero by approximately ±20 pm. In Fig. 2c and 2d, both the mapped deviations $\Delta b_{p,Gd}$ and $\Delta a_{p,Fe}$ do not show any significant deviation. For the deviations $\Delta b_{p,Fe}$, mapped in Fig. 2e, oscillations are noticed in three planes around the TB. As plotted on the right side of the map, the $\Delta b_{p,Fe,10.5}$ and $\Delta b_{p,Fe,12.5}$ are slightly above zero, while the $\Delta b_{p,Fe,11.5}$ is below zero. Individual deviations of $\Delta b_{p,Fe,11.5}$ are plotted in Fig. 2g, indicating an overall reduced b_p between the two Fe rows adjacent to the TB. Moreover, the averaged $\Delta b_{p,Fe}$ in rows #10.5 and 12.5 ($\Delta b_{p,Fe,10.5-12.5}$) are plotted in Fig. 2g as well, which is almost zero. Thus, any significantly distorted b_{p,Fe} is well confined within c.a. two unit cells around the TB. In the vicinity of the TB, as indicated by the arrow in Fig. 2e, some localized deviation of b_{p,Fe} along [100]_L are also noticed, but with a much lower magnitude. The laterally averaged values of Δb_{p,Fe} among the first 14 columns are plotted in Fig. 2h, indicating small deviations also present away from the TB in the L part.

The lattice distortions revealed in Fig. 2 suggest possible spontaneous polarization around the TB. Such well-confined polarization could find use in boosting the performance of ferroelectric devices, as predicted in the case of CaTiO₃.^{10, 12} In order to directly show the existence and determine the magnitude of projected polarization in the material and at the twin boundary, in

addition to Gd and Fe positions, also O positions need to be resolved. Therefore, the iDPC¹⁷ technique was employed, which offers the ability to resolve close light and heavy atoms in the same image. Fig. 3a and 3b show simultaneously acquired HAADF and iDPC images. On both sides of Fig. 3a are the laterally averaged intensity profiles from the two regions defined by the rectangles. As indicated by the arrows, two neighboring Gd {110} planes are giving higher peaks than the others. Thus, similar to the case in Fig. S4, the TB in Fig. 3a shifts by one plane in this area. Fig. 3b is the iDPC image, where planes of the Gd and Fe sub-lattices are labeled separately. The region defined by the rectangle in Fig. 3b is further enlarged in Fig. 3c. When compared with the overlaid GFO model, both Gd and Fe atomic positions can be identified. There are two types of O in the GFO structure. The O₁ sites (orange) located between neighboring Gd positions can be recognized as the weak intensity peaks around each Gd position. The O₂ sites (blue) are only about 50 pm away from the Fe sites, and are not resolved as separated peaks from the strong Fe signal in Fig. 3c.

The Gd, Fe and O_1 positions are first determined. Due to the overlapping of adjacent Gd atomic columns at each Gd position and the unresolvable O_2 sites, direct measuring the Gd off-centering with respect to the Gd polyhedron is challenging. Instead, both the Gd and Fe positions were compared with the four neighboring O_1 sites as indicated by the quadrilaterals in Fig. 3c. The detected off-centering of Gd and Fe (δ_{Gd} and δ_{Fe}) are expected to provide a good reference to indicate the projected polarization. In Fig. 3d-e, the mapped δ_{Fe} and δ_{Gd} are overlaid on the original iDPC image. Local maxima of δ_{Fe} are mainly distributed in the L part, and along the a_L direction, consistent with the small $\Delta b_{p,Fe}$ observed in Fig. 2e and 2h. The averaged δ_{Fe} from each {110} plane is plotted in Fig. 3f, where $\delta_{Fe,xx}$ and $\delta_{Fe,yy}$ are the components along lateral and vertical direction, respectively. In general, both $\delta_{Fe,xx}$ and $\delta_{Fe,yy}$ are detected in the L part. In Fig. 3e, the local maxima of δ_{Gd} are consistently noticed along the TB, and follow the shift of the TB between Gd rows #5 and #6 at column #10 as already observed in the HAADF image. Therefore, dividing the δ_{Gd} map into a left (column #1-10) and a right (column #11-16) part, Fig. 3g plots the averaged δ_{Gd} from each labeled row. The

detected $\delta_{Gd,yy}$ are rather small and randomly jumping around zero. In contrast, we find quite strong cation off-centering of about 30 pm $\delta_{Gd,xx}$ at the TB, i.e. in the Gd row #6 from the left part and in row #5 from the right part.

In addition to the lattice distortion and off-centered cations, chemical disorder around the TB is probed by EELS SI as well. Fig. 4a displays the simultaneously acquired annular dark-field (ADF) image, the extracted elemental maps including the Gd $M_{4.5}$, Fe $L_{2.3}$, O K and Ce $M_{4.5}$ edges, and a composite map of Gd and Fe around the TB. All atomic rows are labeled on the left, where the TB can be located at row #16. The Gd, Fe and O map in Fig. 4a are showing a good agreement with the GFO structure, as well as a quite uniform intensity distribution. In the Ce map, several local maxima are randomly distributed at the Gd sites, as indicated by the two sets of squares placed at the same positions in both Gd and Ce map. Fig. 4b plots the intensity profiles across the TB as obtained by laterally averaging of elemental maps in Fig. 4a. While the intensity of the Fe signal remains almost constant, the signal of Gd and O slightly drops around the TB. The slight drop of O intensity (~2%) is always noticed at the TB without any significant changes in the fine structure of the O K edge, supporting the theory that the TBs represent sinks for oxygen vacancies. 12, 13, 22-24 Along the Ce profile, several peaks are recognizable and coincide with the Gd peaks. Although a hump is noticed around the TB in Fig. 4b, the Ce substitution of Gd is found rather random and independent of the TB when comparing different sample areas, e.g. in Supporting Information, Fig. S7. The bottom plot in Fig. 4b shows the relative thickness (t/λ) profile, which suggests no abrupt thickness variation across the TB.

Moreover, utilizing the fine structure of Ce $M_{4,5}$ edge,²⁵⁻²⁷ the valence state of Ce is determined, and compared in Fig. 4c with the Ce/Gd ratio estimated from each Gd row. Different from the Ce⁴⁺ in the matrix ceria phase, most of the Ce inside C-GFO are Ce³⁺, consistent with the Gd³⁺. Comparing the two curves in Fig. 4c, the Ce valence state increases as the Ce/Gd ratio decreases, and vice versa, suggesting a self-modulation of the overall contribution from Ce. In addition to Ce, the valence-specific multiplet structures of Fe $L_{2,3}$ edges also enable an

estimation of the Fe valence states.^{15, 28} At the bottom of Fig. 4c, the estimated Fe³⁺ fraction (Fe³⁺/ Σ Fe) from each Fe row is plotted. Overall, the Fe³⁺/ Σ Fe is quite constant, and shows ignorable dependence on the TB. From the whole mapped region, an averaged fraction of ~88.5% is determined, indicating that the Fe sites are mainly occupied with Fe³⁺ but also mixed with ~11.5% Fe²⁺. The hopping pairs of Fe²⁺ and Fe³⁺ at the charge-conducting octahedral sites could be then responsible for the electronic conductivity of the material.

In summary, we have directly visualized the atomic structure at the (110) TB of C-GFO with picometer precision. Independent of chemical variations, the formation of the TB caused significant yet well-confined distortions within the Gd sub-lattice, and up to 30 pm off-centering of Gd with respect to the neighboring O was determined. As predicted for the CaTiO₃ case, ¹² a cation off-centering of only 1.5 pm will result in a boundary polarization between 0.004 and 0.02 Clb/m². Thus, considerable spontaneous polarization at the TB is expected in our case, and might be even higher than the bulk spontaneous polarization of BaTiO₃ (0.24 Clb/m²). The Fe sublattice undergoes similar distortions, while only small Fe off-centering is randomly noticed within the bulk region. The observed shift of the TB adds another dimension of flexibility to engineer the boundaries, i.e. the length and shape of the TB can be tailored to some degree.²⁹ Consistent with the theory, slight accumulation of oxygen vacancies at the TB was also revealed by chemical analysis. Our results here are essential for designing boundaries with superior properties, controlling their distributions, and finally creating materials that contain localized functionalities such as superconductivity and ferroelectricity, even when such effects do not exist in the bulk.

Acknowledgement

This work has been supported by the Deutsche Forschungsgemeinschaft (Project number 387282673). KR acknowledges support by the Bundesministerium für Bildung und Forschung (NEUROTEC, 16ME0399 and 16ME0398K). The author thank Maximilian Kruth

(Forschungszentrum Jülich) for the preparation of the TEM lamellae, and Penghan Lu (Forschungszentrum Jülich) for valuable discussions.

Associated Information

Notes: The authors declare no competing interests.

Supporting Information is available

Detailed methods, diffraction patterns from the C-GFO grain, determination of the ellipticity at each Gd position, construction of the TB model and the HAADF image simulation, shift of the TB, and EELS mapping from different area of the TB.

Reference

- 1. Salje, E. H. K., Multiferroic domain boundaries as active memory devices: trajectories towards domain boundary engineering. *Chemphyschem* **2010**, *11*, 940-950.
- 2. Aird, A.; Salje, E. H. K., Sheet superconductivity in twin walls: experimental evidence of WO_{3-x}. *J Phys-Condens Mat* **1998**, *10*, 377-380.
- 3. Campanini, M.; Erni, R.; Yang, C. H.; Ramesh, R.; Rossell, M. D., Periodic Giant Polarization Gradients in Doped BiFeO₃ Thin Films. *Nano Lett* **2018**, *18*, 717-724.
- 4. Wu, X. F.; Rabe, K. M.; Vanderbilt, D., Interfacial enhancement of ferroelectricity in CaTiO₃/BaTiO₃ superlattices. *Phys Rev B* **2011**, *83*, 020104.
- 5. Kim, Y. M.; Morozovska, A.; Eliseev, E.; Oxley, M. P.; Mishra, R.; Selbach, S. M.; Grande, T.; Pantelides, S. T.; Kalinin, S. V.; Borisevich, A. Y., Direct observation of ferroelectric field effect and vacancy-controlled screening at the BiFeO₃/LaxSr_{1-x}MnO₃ interface. *Nat Mater* **2014**, *13*, 1019-1025.
- 6. Jia, C. L.; Nagarajan, V.; He, J. Q.; Houben, L.; Zhao, T.; Ramesh, R.; Urban, K.; Waser, R., Unit-cell scale mapping of ferroelectricity and tetragonality in epitaxial ultrathin ferroelectric films. *Nat Mater* **2007**, *6*, 64-69.
- 7. Jin, L.; Xu, P. X.; Zeng, Y.; Lu, L.; Barthel, J.; Schulthess, T.; Dunin-Borkowski, R. E.; Wang, H.; Jia, C. L., Surface reconstructions and related local properties of a BiFeO₃ thin film. *Sci Rep-Uk* **2017**, *7*, 39698.
- 8. Zykova-Timan, T.; Salje, E., Highly mobile vortex structures inside polar twin boundaries in SrTiO₃. *Appl Phys Lett* **2014**, *104*, 082907.
- 9. Tagantsev, A. K.; Courtens, E.; Arzel, L., Prediction of a low-temperature ferroelectric instability in antiphase domain boundaries of strontium titanate. *Phys Rev B* **2001**, *64*, 224107.
- 10. Van Aert, S.; Turner, S.; Delville, R.; Schryvers, D.; Van Tendeloo, G.; Salje, E. K. H., Direct Observation of Ferrielectricity at Ferroelastic Domain Boundaries in CaTiO₃ by Electron Microscopy. *Adv Mater* **2012**, *24*, 523-527.
- 11. Yokota, H.; Usami, H.; Haumont, R.; Hicher, P.; Kaneshiro, J.; Salje, E. K. H.; Uesu, Y., Direct evidence of polar nature of ferroelastic twin boundaries in CaTiO₃ obtained by second harmonic generation microscope. *Phys Rev B* **2014**, *89*, 144109.
- 12. Goncalves-Ferreira, L.; Redfern, S. A. T.; Artacho, E.; Salje, E. K. H., Ferrielectric twin walls in CaTiO₃. *Phys Rev Lett* **2008**, *101*, 097602.

- 13. Lee, W. T.; Salje, E. K. H.; Bismayer, U., Influence of point defects on the distribution of twin wall widths. *Phys Rev B* **2005**, *72*, 104116.
- 14. Buchheit, A.; Tessmer, B.; Ran, K.; Mayer, J.; Wiemofer, H. D.; Neuhaus, K., The impact of Fe addition on the electronic conductivity of Gadolinium doped ceria. *Ecs J Solid State Sc* **2019**, *8*, 41-50.
- 15. Ran, K.; Zeng, F. L.; Fischer, L.; Baumann, S.; Meulenberg, W. A.; Neuhaus, K.; Mayer, J., The in situ generated emerging phase inside dual phase oxygen transport membranes. *Acta Materialia* **2022**, *234*, 118034.
- 16. Ross, N. L.; Zhao, J.; Angel, R. J., High-pressure structural behavior of GdAlO₃ and GdFeO₃ perovskites. *J Solid State Chem* **2004**, *177*, 3768-3775.
- 17. Yucelen, E.; Lazic, I.; Bosch, E. G. T., Phase contrast scanning transmission electron microscopy imaging of light and heavy atoms at the limit of contrast and resolution. *Sci Rep-Uk* **2018**, *8*, 2676.
- 18. Nord, M.; Vullum, P. E.; MacLaren, I.; Tybell, T.; Holmestad, R., Atomap: a new software tool for the automated analysis of atomic resolution images using two-dimensional Gaussian fitting. *Advanced Structural and Chemical Imaging* **2017**, *3*, 9.
- 19. Barthel, J., Dr. Probe: A software for high-resolution STEM image simulation. *Ultramicroscopy* **2018**, *193*, 1-11.
- 20. Jia, C. L.; Mi, S. B.; Urban, K.; Vrejoiu, I.; Alexe, M.; Hesse, D., Atomic-scale study of electric dipoles near charged and uncharged domain walls in ferroelectric films. *Nat Mater* **2008**, *7*, 57-61.
- 21. Gonnissen, J.; Batuk, D.; Nataf, G. F.; Jones, L.; Abakumov, A. M.; Van Aert, S.; Schryvers, D.; Salje, E. K. H., Direct Observation of Ferroelectric Domain Walls in LiNbO₃: Wall-Meanders, Kinks, and Local Electric Charges. *Adv Funct Mater* **2016**, *26*, 7599-7604.
- 22. Goncalves-Ferreira, L.; Redfern, S. A. T.; Artacho, E.; Salje, E.; Lee, W. T., Trapping of oxygen vacancies in the twin walls of perovskite. *Phys Rev B* **2010**, *81*, 024109.
- 23. Calleja, M.; Dove, M. T.; Salje, E. K. H., Trapping of oxygen vacancies on twin walls of CaTiO₃: a computer simulation study. *J Phys-Condens Mat* **2003**, *15*, 2301-2307.
- 24. Lee, W. T.; Salje, E. K. H.; Goncalves-Ferreira, L.; Daraktchiev, M.; Bismayer, U., Intrinsic activation energy for twin-wall motion in the ferroelastic perovskite CaTiO₃. *Phys Rev B* **2006**, *73*, 214110.
- 25. Fortner, J. A.; Buck, E. C., The chemistry of the light rare-earth elements as determined by electron energy loss spectroscopy. *Appl Phys Lett* **1996**, *68*, 3817-3819.
- 26. Yan, P. F.; Mori, T.; Wu, Y. Y.; Li, Z. M.; Auchterlonie, G. J.; Zou, J.; Drennan, J., Microstructural and Chemical Characterization of Ordered Structure in Yttrium Doped Ceria. *Microsc Microanal* **2013**, *19*. 102-110.
- 27. Ran, K.; Fischer, L.; Baumann, S.; Meulenberg, W. A.; Neuhaus, K.; Mayer, J., Tuning the ceria interfaces inside the dual phase oxygen transport membranes. *Acta Materialia* **2022**, *226*, 117603.
- 28. van Aken, P. A.; Liebscher, B., Quantification of ferrous/eerric ratios in minerals: new evaluation schemes of Fe L_{23} electron energy-loss near-edge spectra. *Phys Chem Miner* **2002**, *29*, 188.
- 29. Salje, E. K. H., Ferroelastic Materials. *Annu Rev Mater Res* **2012**, *42*, 265-283.

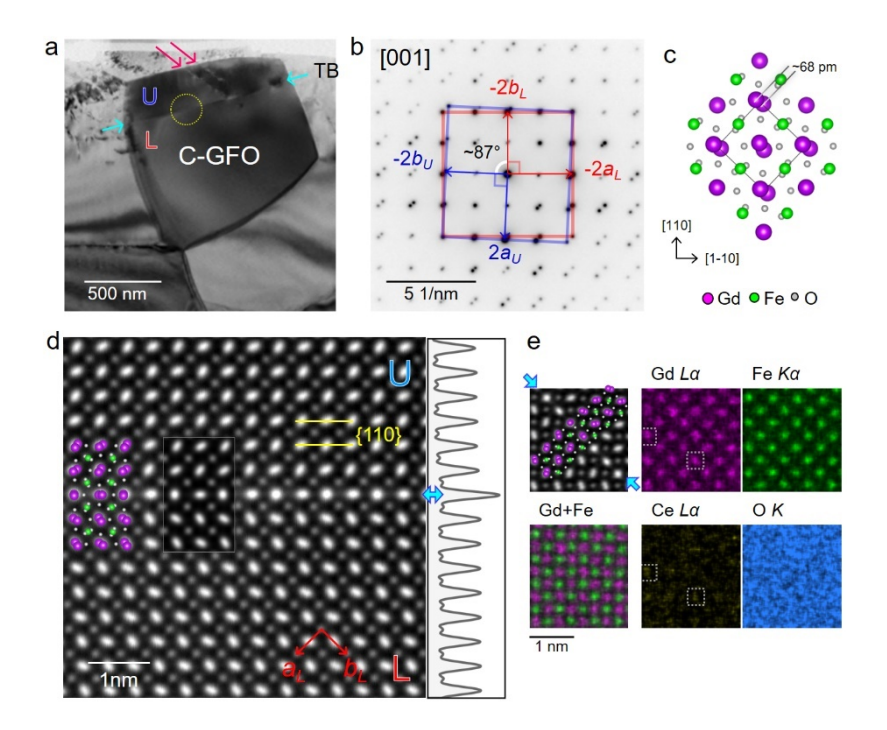


Fig. 1 The C-GFO grain with TB. (a) TEM bright field image showing a single C-GFO grain surrounded by the ceria host phase. As indicated by the pair of arrows in cyan, the twin boundary (TB) shows a similar contrast as the surroundings, goes through the C-GFO grain, and separates the grain into an upper (U) and a lower (L) part. Additional stacking faults are indicated by the two arrows in pink. (b) Diffraction pattern acquired from the region marked by the dotted circle in (a). Two patterns with a relative rotation of ~87° are outlined by the blue and red rectangles. Both patterns correspond to the [001] direction of GFO. (c) The GFO model viewed along [001] direction. A single unit cell is indicated by the rectangle. (d) HAADF image showing the atomic structure around the TB. A proposed structural model together with the simulated HAADF image are overlaid on the image. The plot on the right is the intensity profile, obtained by laterally averaging the HAADF image. (e) EDX chemical mapping results around the TB: The HAADF image, the elemental maps in intensity from the Gd $L\alpha$ line, Fe $K\alpha$ line, Ce $L\alpha$ line and O K line, together with a composite map of Gd and Fe. For the HAADF image in (e), the TB is indicated by the arrows and the proposed model as in (d) is overlaid. A set of two squares is placed at the same position in the Gd and Ce map, showing that peaks of Ce signal correlate to those of Gd in the respective maps.

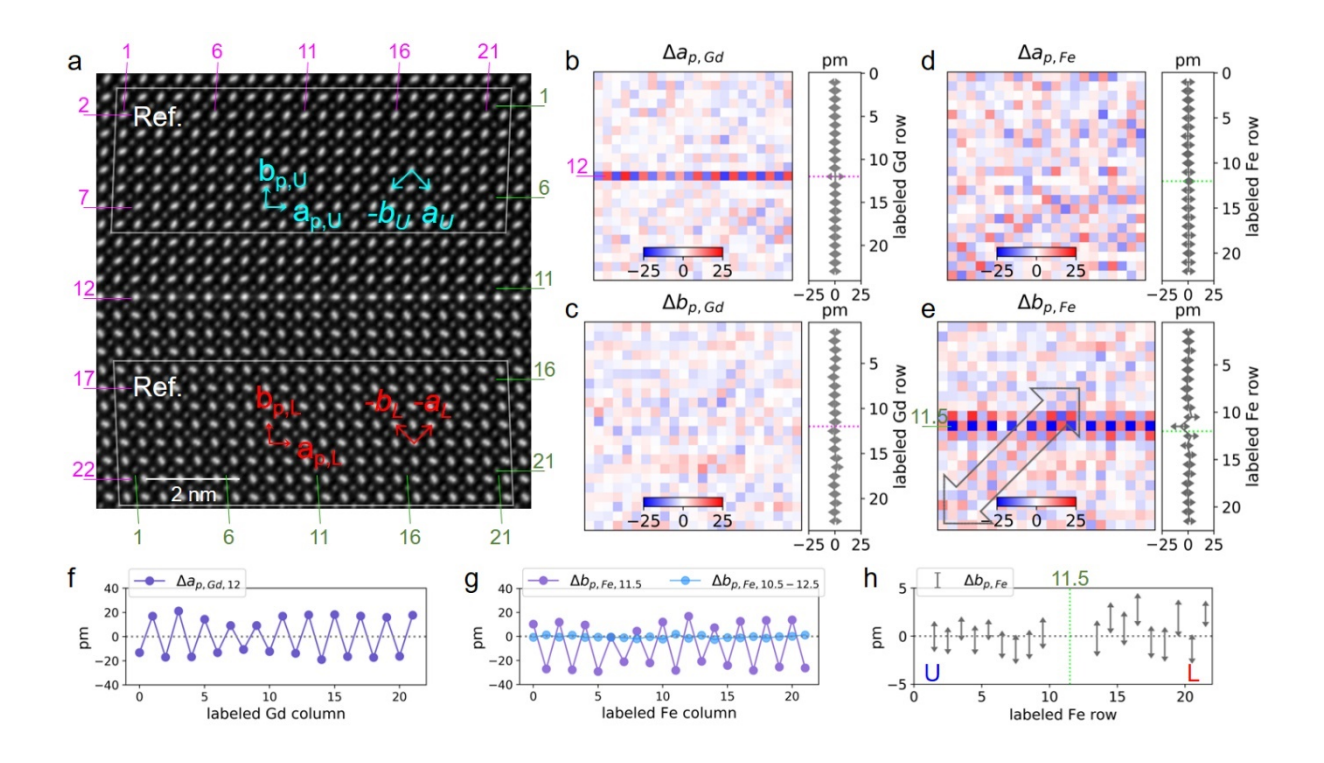


Fig. 2 Lattice distortion within the Gd and Fe sublattice. (a) HAADF image of the TB. The Gd and Fe sub-lattices are labeled separately, and the pseudo lattice constants a_p and b_p are defined. (b-e) Deviation matrices of Δa_p and Δb_p from the Gd and Fe sub-lattice in (a), by taking the two outlined bulk regions as a reference. On the right side of each map are the averaged values from each labeled row. (f) The extracted deviation $\Delta a_{p,Gd}$ from Gd row #12, $\Delta a_{p,Gd,12}$. (g) The extracted deviation $\Delta b_{p,Fe}$ from Fe row #11.5, $\Delta b_{p,Fe,11.5}$, and the averaged $\Delta b_{p,Fe}$ for Fe rows #10.5-12.5, $\Delta b_{p,Fe,10.5-12.5}$. (h) The laterally averaged $\Delta b_{p,Fe}$ among the first 14 Fe columns. The values from Fe row #10.5-12.5 are not shown.

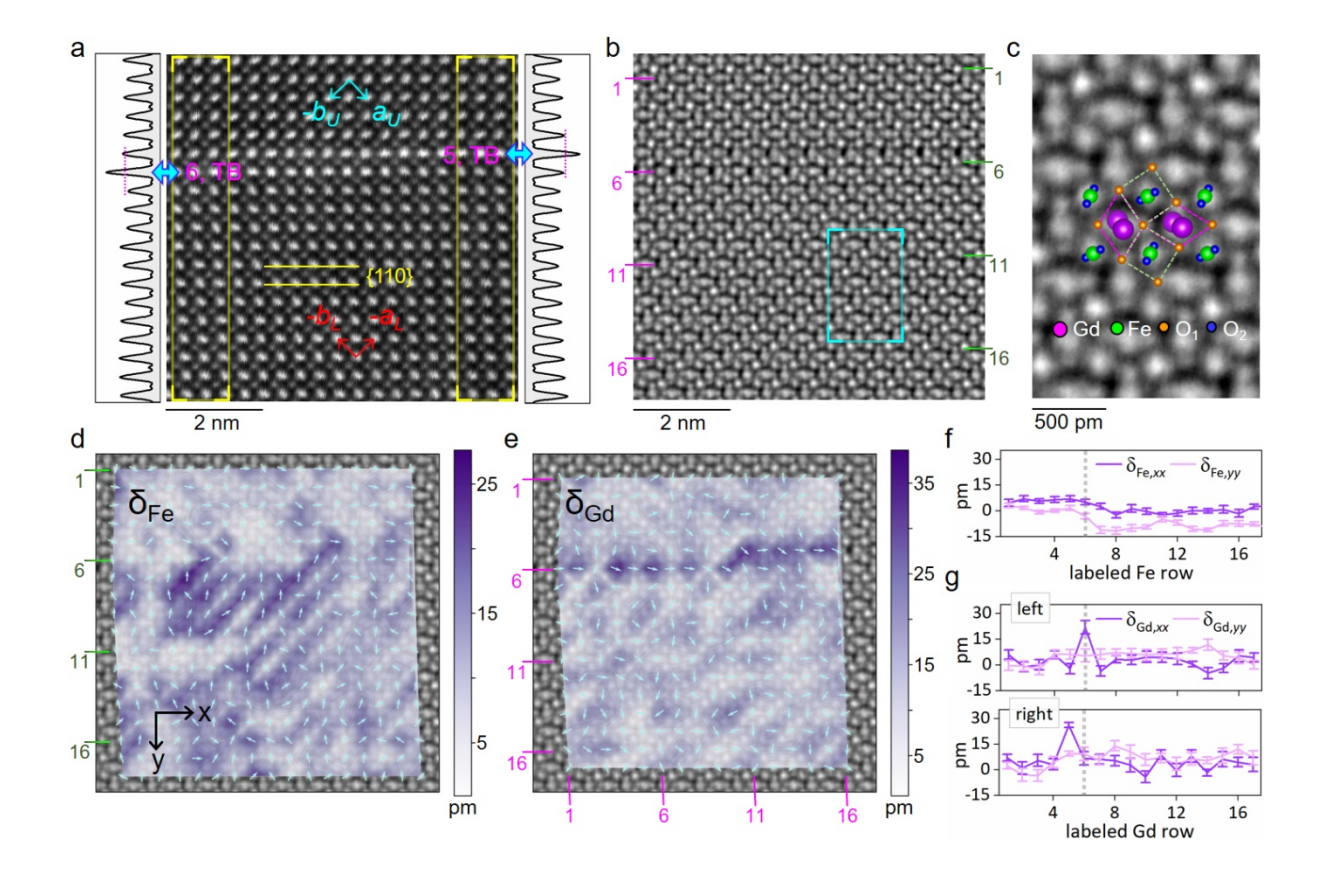


Fig. 3 Off-centering of Gd and Fe. (a-b) the simultaneously acquired HAADF and iDPC images. On both sides of (a) are the laterally averaged intensity profiles from the two regions defined by the rectangles. The TB shifts by one plane as indicated by the two arrows. (c) The enlarged image from the region defined by the rectangle in (b). Part of the GFO structural model is overlaid on the image. (d-e) Maps of the off-centering of Fe and Gd (δ_{Fe} and δ_{Gd}) with respect to the neighboring four O₁ sites, as outlined by the quadrilaterals in (c). Background is the iDPC image in (b) for comparison. (f) The averaged δ_{Fe} along x and y direction, $\delta_{Fe,xx}$ and $\delta_{Fe,yy}$, from each labeled Fe row. (g) Top: the averaged $\delta_{Gd,xx}$ and $\delta_{Gd,yy}$ from each labeled Gd row among the left part (Gd column #1-10); bottom: the averaged $\delta_{Gd,xx}$ and $\delta_{Gd,yy}$ from each labeled Gd row among the right part (Gd column #11-16).

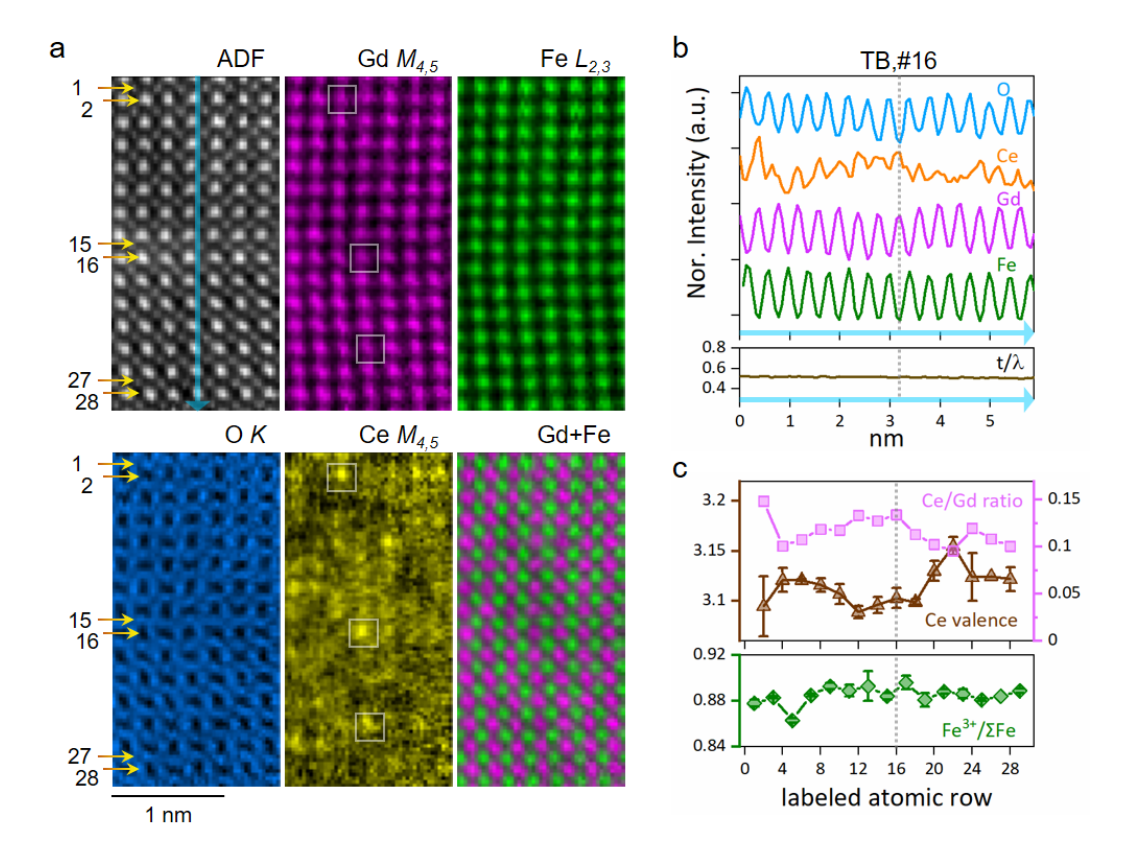


Fig. 4 Chemical structure around the TB. (a) EELS SI results: simultaneously acquired ADF image and elemental maps plotting the intensity from the Gd $M_{4,5}$, Fe $L_{2,3}$, O K, and Ce $M_{4,5}$ edges, together with a composite map of Gd and Fe. Each atomic row is labeled on the left side, and the TB is located at row #16. Two sets of squares placed at the identical positions in the Gd and Ce maps, indicate that peaks in the Ce signal occur at Gd positions. (b) Intensity profiles by laterally averaging the elemental maps in (a). The estimated relative sample thickness, t/λ, based on low-loss SI is also plotted at the bottom. (c) The estimated Ce/Gd intensity ratio, Ce valence state, and Fe³⁺/ΣFe from the corresponding atomic rows. The TB is indicated by the dotted lines.

Table of Contents

